Mechanical Properties and Failure Behaviour of Architected Alumina Microlattices Fabricated by Stereolithography 3D Printing

Xiu Yun Yap[1,2,#], Ian Seetoh[1,#], Wei Liang Goh[1], Pengcheng Ye[3], Yida Zhao[2], Zehui Du[1,*], Chang Quan Lai[1,*], Chee Lip Gan[1,2,*]

[1] Temasek Laboratories, Nanyang Technological University, 50 Nanyang Drive, Singapore 637553

[2] School of Materials Science and Engineering, Nanyang Technological University, Nanyang Avenue, Singapore 639798

[3] Creatz3D Pte Ltd, 180 Paya Lebar Road, Singapore,409032

[#]Authors contributed equally to this work.

ABSTRACT

Alumina microlattices with solid struts and different topologies were fabricated by the stereolithography 3D printing method. Mechanical analysis shows that specific stiffness and strength were highest for Simple Cubic lattices, followed by Octet Truss, then Kelvin Cell lattices. The mechanical properties followed Ashby's power law well at small relative densities (≤ 0.3), but deviated from it at higher relative densities due to the increased importance of joint deformation. Failure in the Simple Cubic lattices proceeded in a column-by-column manner from the boundaries inwards to the centre, while fracture in Octet Truss and Kelvin Cell lattices took place predominantly along the diagonal (110) plane. The underlying mechanism controlling these mechanical responses has been thoroughly discussed using finite element simulation analysis. Because lattice strength was limited by the tensile strength of alumina, which was an order of magnitude lower than its compressive strength, the microlattices were weaker than Ashby's predictions. Nevertheless, they were still able to exhibit better specific

* Corresponding authors: Zehui Du (duzehui@ntu.edu.sg); Changquan Lai (cqlai@ntu.edu.sg); Chee Lip Gan (clgan@ntu.edu.sg)

modulus and strength than many current engineering materials, as well as some degree of ductility in the form of pseudoplastic strains (0.1 % - 0.5 %).

Key words: Microlattice; Alumina, topology; relative density, mechanical properties

1. INTRODUCTION

Micro-/ nano- lattices have attracted much attention in recent years due to their superior mechanical properties over bulk materials, which include enhanced toughness, deformation recoverability, vibration/ shock/ acoustic damping and thermal insulation properties [1–3]. They are essentially porous materials that have been precisely engineered through the tessellation of unit cells, which consist of basic elements such as struts and joints. Some lattice designs commonly found in the literature are the Simple cubic, Octet Truss and Kelvin Cell (*i.e.* tetrakaidecahedron) geometries [4–7].

The mechanical properties of a lattice depend mainly on its constituent material, geometrical design and relative density, $\frac{\rho}{\rho_s}$, where ρ refers to the density of the lattice and ρ_s refers to the density of the constituent material. If the lattice is constructed from a single homogeneous material, $\frac{\rho}{\rho_s}$ can also be taken as the solid fraction of the lattice. Following Ashby's classic analysis, the Young's modulus, *E*, and failure strength, σ_y, of a lattice can be correlated to its relative density with the following relationships: $E/E_s \propto (\frac{\rho}{\rho_s})^n$ and $\sigma_y/\sigma_{ys} \propto (\frac{\rho}{\rho_s})^n$, where *s* refers to the solid constituent material [8]. The exponent, *n*, is determined by the topology of the lattice. For a stretch-dominated lattice, such as the Octet Truss design, $n = 1$ (*i.e.* $E/E_s \propto \frac{\rho}{\rho_s}$ and $\sigma_y/\sigma_{ys} \propto \frac{\rho}{\rho_s}$) [8]. A bending-dominated geometry, such as the Kelvin Cell, on the other hand, would have $n = 2$ for the modulus-density relationship (*i.e.* $E/E_s \propto (\frac{\rho}{\rho_s})^2$) and $n = 1.5$ for the strength-density relationship (*i.e.* $\sigma_y/\sigma_{ys} \propto (\frac{\rho}{\rho_s})^{1.5}$) [8]. In general, stretch-dominated lattices possess high specific elastic moduli while bending-dominated lattices tend to exhibit a long plateau stress in the post-failure regime that lends itself to excellent energy absorption efficiencies [9].

To date, most of the micro-/nano- lattices that have been studied in detail are fabricated from ductile materials, including metal, polymers and their composites. For instance, Mazur *et al.* [10] synthesized Body-Centred Cubic (BCC) and Face-Centred Cubic (FCC) microlattices with relative densities of 0.05 - 0.40 from Ti6Al4V and AlSi12Mg alloys, Tancogne-Dejean *et al.* [11] and Al-Ketan *et al.* [4] produced Kelvin cell, Octet Truss and Gibson-Ashby microlattices with relative density of 0.10 - 0.30 from steel, and Chen *et al*. [12] prepared Octet Truss lattices with relative density of ~ 0.10 - 0.40 from acrylate polymers.

Ceramic lattices, in contrast, have not been as well-studied, partly because additive manufacturing of ceramics remains technically challenging. Therefore, the synthesis of most ceramic micro-/ nano- lattices in the literature relies on indirect methods, such as coating a thin film of alumina onto a polymeric lattice template [3,13]. For instance, Meza *et al.* [3] and Zheng *et al.* [13] deposited thin films of alumina onto polymer lattices which were subsequently removed through plasma etching to form extremely lightweight hollow-tube alumina Octet Truss micro-/nano- lattices with relative densities in the range of ~ 0.0004 - 0.10. The Young's modulus of such lattices were observed to scale with relative density in the form of $E \propto \rho$ or $E \propto \rho^{1.61}$, while failure strength scaled as $\sigma_f \sim \rho^{1.6-2.7}$, which differed from the analytical scaling for solid-strut lattices [8]. Furthermore, hollow-tube nanolattices with a wall thickness of ~10 nm were observed to exhibit an elastic-ductile behaviour with recoverable strains of up to 50%, while thick-walled lattices with a relative density of 0.02 - 0.10 tend to exhibit catastrophic failure, with the struts fracturing discretely.

Attempts to fabricate ceramic lattices with solid struts, on the other hand, are currently limited to the use of polymer-derived ceramics [14–16]. Typically, a photosensitive mixture containing organic and inorganic groups is selectively exposed to light, layer-by-layer, using the stereolithography or 2-photon polymerization technique to form a 3D structure. The structure will then be pyrolyzed at high temperatures, leaving behind only the inorganic

(ceramic) material in the lattice. While fully densified struts can be obtained with this approach, designing the photosensitive mixture is not trivial, and only limited materials, such as silicon oxycarbide [14,15] and titania [16], have been demonstrated thus far. Stereolithography 3D printing of an alumina-binder suspension, followed by a high temperature treatment to remove the binder, was also attempted previously [17], but the porosity of the resultant material was 84%, and silicon carbide had to be coated onto the alumina lattices to seal the pores before the lattices could be mechanically characterized.

As a result of these challenges, information on the elastic and fracture behaviour of additively manufactured, homogeneous (*i.e.* single-material) ceramic lattices with solid struts, particularly those not fabricated from silicon oxycarbide, remain relatively scarce [17,18]. Furthermore, much of the current studies are focused on ceramic lattices with extremely small strut diameters ($\leq 20\mu m$), where defects in the constituent ceramics are minimized, if not eliminated completely, leading to unparalleled stiffness, strength and ductility [14,19–23]. While these properties are exciting and much sought-after, there is limited scalability to the methods used to fabricate these lattices. For instance, it takes days to produce a 1 mm x 1 mm x 1 mm lattice using 2-photon polymerization and successful post-printing steps such as atomic layer deposition and plasma etching have yet to be demonstrated beyond micro-/nano-scale lattices.

To address this gap in knowledge, we first shaped microlattices into the Simple Cubic, Octet Truss and Kelvin Cell designs through direct stereolithography 3D printing of an alumina-binder paste and then sintered the lattices at high temperature (~ 1700 °C). This method can be used to produce lattices of size 100 mm x 100 mm x 100 mm and beyond, although structures that were 20 mm x 20 mm x 20 mm and smaller were sufficient for the present study. The diameter of the fully dense lattice struts was 0.5 mm (Supplementary Information, Table S1, Figure S1 & Figure S3), and their lengths were varied so that the relative

density ranged from 0.10 to 0.50 (*i.e.* 0.3 - 1.8 g/cm^3). A series of quasi-static compression tests were conducted on the lattices, and the deformation process was captured with a high-speed camera, with frame rates up to 50,000 fps. Local strains in the lattices were measured through Geometrical Phase Analysis of the high-speed camera images and finite element analysis was also performed and compared to the experimental results to uncover the deformation and failure mechanisms.

2. MATERIALS AND METHODS

2.1. Fabrication of alumina lattices

Solidworks® (Dassault Systèmes) was used to design Octet Truss (Figure 1A), Kelvin Cell (Figure 1B) and Simple Cubic lattices (Figure 1C) of different relative densities (ρ/ρ_s). Figure 1(A) – (C) shows examples of the Solidworks lattice models (ρ/ρ_s = 0.3). Each lattice was made up of 4 x 4 x 4 unit cells. To vary the relative density, the strut diameter (d) was kept constant at 0.5 mm while the strut length (l) was changed. Increasing the strut length reduced the relative density. Table 1 shows the geometric parameters of the various lattice structures fabricated in this work.

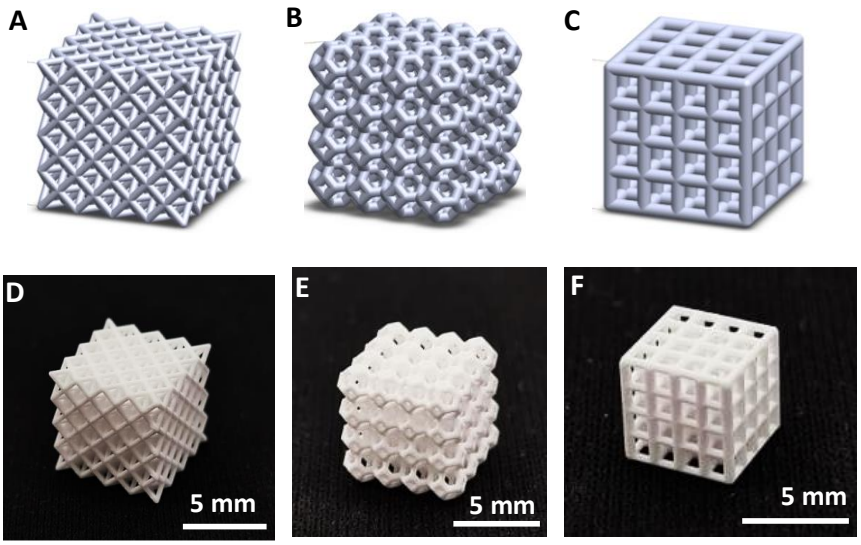

Figure 1: Solidworks® models of 4 x 4 x 4 (A) Octet Truss lattice, (B) Kelvin Cell lattice and (C) Simple Cubic lattice with ρ/ρ_s = 0.3. Photos of the 3D printed and sintered ceramic microlattices (ρ/ρ_s = 0.3) of (D) Octet Truss, (E) Kelvin Cell and (F) Simple Cubic lattices.

The lattices were 3D printed by the stereolithography technique using Ceramaker C900 FLEX printer (3DCeram, France). A UV laser with a wavelength of 355 nm was used to cure a commercial paste (3DMIX, Alumina) that consisted of alumina powder and a photosensitive polymer resin [24]. The curing was conducted layer by layer, according to an input design, to

give the 3D structures. After printing, uncured paste was removed through the pressurized spraying of the Ceraclean solution (3DCeram). The compressed air pressure used (5 bar) had been optimized to remove the uncured paste efficiently while avoiding damages to the green bodies, which were then debinded and sintered at 1700°C.

Compressive tests performed on solid alumina fabricated this way revealed a compressive strength of 2.3 GPa and Young's modulus of 318 GPa. Flexural tests, on the other hand, indicated that the tensile strength of the 3D printed alumina was only 0.3 GPa (Supplementary Information, Figure S2).The compressive strength was slightly lower than the expected value of 2.7 GPa, likely because of the presence of a small amount of pores in the alumina struts (~ 4.5%; Table S1 in Supplementary Information). Our analysis in the following will adopt the lowered value of 2.3 GPa, to account for this porosity.

Figure 1(D) – (F) show the images of the ceramic microlattices with ρ/ρ_s = 0.3 after sintering. The actual size of the three lattices was close to the designed dimensions, with a deviation of ± 0.1 - 1%, according to micro-CT scans shown in Figure S3 in Supplementary Material.

Table 1: Geometric parameters of respective lattice structures used in this study. Note that the relative density of the Kelvin Cell lattice could not be increased beyond 0.3 as it would become a closed-cell geometry.

Lattice type	**Strut Diameter (mm)**	**Strut Length (mm)**	**lattice dimension (length x width x height) Unit: mm**	**Relative Density (ρ/ρ_s)**
Octet Truss	0.5	3.0	17.50 x 17.50 x 17.50	0.15
		2.50	14.70 x 14.70 x 14.70	0.20
		2.0	11.80 x 11.80 x 11.80	0.30
		1.75	10.40 x 10.40 x 10.40	0.40
		1.50	8.98 x 8.98 x 8.98	0.50
Kelvin Cell	0.5	1.0	11.70 x 11.70 x 11.70	0.15
		0.80	9.54 x 9.54 x 9.54	0.20
		0.70	8.40 x 8.40 x 8.40	0.30
Simple Cubic	0.5	2.50	10.50 x 10.50 x 10.50	0.10
		1.80	7.70 x 7.70 x 7.70	0.20

	1.35	5.90 x 5.90 x 5.90	0.30
	1.15	5.10 x 5.10 x 5.10	0.40
	0.95	4.10 x 4.10 x 4.10	0.50

2.2. Characterization

Quasi-static compression test was conducted using Instron 5567 equipped with a 10 kN load cell. The compressive strain rate was set as 0.001 s^{-1} and at least 5 samples were tested for each geometry to obtain an average result. To study the fracture behaviour of the lattice structures, high speed videos were taken during the compression tests using FASTCAM Mini AX200 camera (Photron, Japan) at a frame rate up to 50,000 fps. The video resolution was 256 pixels x 256 pixels. Images of the lattice at the start of compression test and right before catastrophic failure were extracted from the video and analyzed for strain using the Graphic Phase Analysis (GPA) method [25–27]. It first involved processing the images with ImageJ to remove the background and account for lighting artifacts. Images in spatial domain were then converted to frequency domain by using Fast Fourier Transform (FFT) algorithm. Gaussian masks were applied to frequency domain to extract displacement information in the directions of interest. The resultant displacement fields were then visualized by plotting the magnitude of the imaginary component of reverse-FFT of the masked frequency domain images. By using the image prior to compression as a reference, local strain fields in the X and Y directions could be computed in MatLab software.

2.3. Simulations

Finite element analysis was performed on the lattice models using Abaqus CAE software package together with the dynamic explicit solver. The "non-linear geometry" option was selected for these simulations. Each model geometry was a 2 x 2 x 2 lattice of length L, positioned where one of the corners coincided with the origin ($x = y = w = 0$) and (u, v, w)

being the corresponding nodal displacements. Symmetry boundary conditions were prescribed at the *X*, *Y* and *Z* faces (*i.e.* $u|_{x=0} = v|_{y=0} = w|_{z=0} = 0$) to replicate the behaviour of a 4 x 4 x 4 lattice. In this way, the solution was achieved in a more computationally efficient manner.

The lattice models were meshed using quadratic tetrahedral 3D stress elements with characteristic lengths smaller than 1/3 of the strut diameter. Quasi-static uniaxial compression up to strain ε_c was performed by prescribing displacements of $[u = 0, v = \varepsilon_c L, w = 0]$ at $y = L$, along with a 'smooth-step' amplitude function that gradually increased the strain rate from 10^{-7} s^{-1} to 10^{-1} s^{-1}. Compared to linear ramps commonly used elsewhere, the smooth step used here was able to reproduce quasi-static conditions over a much shorter simulation time. Stress data were obtained by measuring the reaction forces during the compression step. Some simulations were repeated, but with the prescribed displacement on the compressing surface modified to enable unconstrained lateral movement of the compressing surface (i.e. $v = \varepsilon_c L$ with u and w not defined). These results are labelled as 'no lateral constraints' in Figure 3, Figure 5 and Figure 6 in the following sections.

The model was assigned an isotropic elastic material with Young's modulus = 318 GPa and Poisson's ratio = 0.242. The former value was obtained from our uniaxial compressive tests on a bulk sample of 3D printed alumina, while the latter was based on manufacturer's (3D Ceram) technical specifications. The "Brittle Cracking" model in Abaqus was used to simulate the failure behaviour based on the Rankine criterion, which assumes that crack formation in brittle materials (*e.g.* concrete and ceramics) is triggered when the maximum principle tensile stress exceeds the material tensile strength [28–30]. Here, the tensile strength of alumina was assigned a value of 300 MPa based on our flexural (three-point bending) tests on 3D printed alumina bars. These tests also showed that bulk alumina failed very abruptly with very little post-failure characteristics (see Figure S2 in Supplementary Material). Accordingly, the post-failure direct stress and the shear retention factor were configured to fall rapidly to zero (*i.e.* by

setting their corresponding post-failure strains to ~ 0). Element deletion was activated to prevent excessive local deformation speeds from interrupting the explicit solver prematurely.

3. RESULTS

3.1. Modulus and strength properties

The modulus, E, and compressive strength, σ_c, of the alumina microlattices obtained from simulations (solid data points) and experiments (hollow data points) are presented in Figure 2. E and σ_c are normalized against the modulus, E_s (= 318 GPa), and the compressive strength, σ_{cs} (= 2.3 GPa), of solid alumina to obtain the relative modulus (E/E_s) and relative strength (σ/σ_{cs}). The strength of the microlattice was taken to be the maximum stress sustained by the lattice right before catastrophic failure. It can be observed that there is excellent agreement between the simulation and experimental data across the different topologies for all relative densities. This implies that any physical deviations of the actual microlattices from the simulation models, such as the presence of small amounts of surface roughness (Figure S1 in Supplementary Information), did not significantly influence their mechanical properties, which were primarily determined by the lattice design and relative density.

Figure 2 shows that both the modulus and strength of the microlattices increase with relative density for all the three geometries. For the same relative density, the relative modulus and relative strength of the microlattices decreased in the order of Simple Cubic > Octet Truss > Kelvin Cell. The Simple Cubic lattice was the stiffest because 1/3 of its struts were aligned along the loading direction, so that the overall lattice deformation was restricted only to axial strain, the most efficient load bearing mode. Within the vertical struts subjected to axial deformation, the stress distribution was generally very even (refer to the Von Mises stress

distribution in the lattices shown in the insets of Figure 2A and 2D), which allowed the Simple Cubic structure to be strong.

In contrast, the struts in Octet Truss and Kelvin Cell were oriented at an angle to the loading direction, so that a uniaxial load would generate moments, and consequently, bending in the struts, leading to less efficient load bearing. The bending also led to stress concentrations on the surface of the struts, where the bending moments were high (insets in Figure 2B, 2C, 2E and 2F), resulting in structures that were relatively less strong. Despite the low loading efficiency in any particular direction, however, cellular structures with slanted struts can offer better isotropy in mechanical properties, as the diagonal struts can sustain similar stresses from multiple directions due to the nature of their orientation [31].

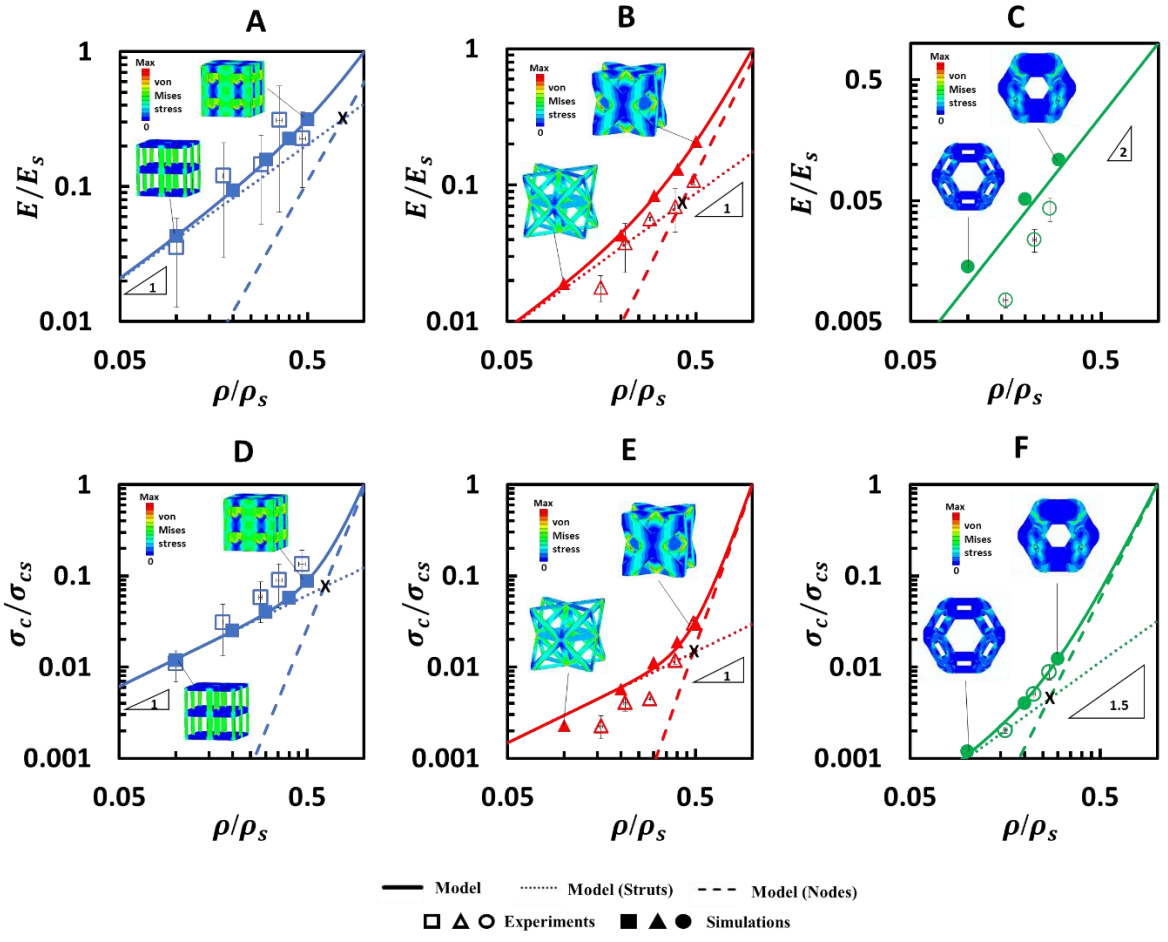

Figure 2: (A-C) Relative modulus and (D-F) relative strength of the Simple Cubic, Octet Truss, and Kelvin Cell lattices as a function of relative density. The contributions by struts (1st term of Eq. 3 to 6) and joints (2nd term of Eq. 3 to 6) are represented by the dotted and dashed lines respectively, with the intersection point indicated by 'x'. Each minor tick in the abscissa (*x*-axis) represents a value of 0.05.

To better understand the correlation between the relative density and the relative modulus, as well as relative strength, the simulation data were fitted with modified Ashby relationships,

$$\frac{E}{E_s} = a\left(\frac{\rho}{\rho_s}\right)^n + (1-a)\left(\frac{\rho}{\rho_s}\right)^m \quad (1)$$

and

$$\frac{\sigma_c}{\sigma_{cs}} = a\left(\frac{\rho}{\rho_s}\right)^n + (1-a)\left(\frac{\rho}{\rho_s}\right)^m \quad (2)$$

with m being a fitting parameter, while a ($0 \leqslant a \leqslant 1$) and n are constants that had been analytically derived previously [31]. Following Ashby's classic analysis, for low relative density materials where the mechanical response is dictated solely by the extent of strut deformation, $n = 1$ for Eq. (1) and (2) for stretch-dominated designs, such as Octet Truss and Simple Cubic, whereas for bending-dominated designs, such as Kelvin Cell, $n = 2$, $a = 1$ for Eq. (1) and $n = 1.5$. for Eq. (2) [8]. In other words,

$$\frac{E}{E_s} = a\left(\frac{\rho}{\rho_s}\right) + (1-a)\left(\frac{\rho}{\rho_s}\right)^m \quad \text{(modulus, stretch-dominated),} \quad (3)$$

$$\frac{\sigma_c}{\sigma_{cs}} = a\left(\frac{\rho}{\rho_s}\right) + (1-a)\left(\frac{\rho}{\rho_s}\right)^m \quad \text{(strength, stretch-dominated),} \quad (4)$$

$$\frac{E}{E_s} = \left(\frac{\rho}{\rho_s}\right)^2 \quad \text{(modulus, bending-dominated),} \quad (5)$$

$$\frac{\sigma_c}{\sigma_{cs}} = a\left(\frac{\rho}{\rho_s}\right)^{3/2} + (1-a)\left(\frac{\rho}{\rho_s}\right)^m \quad \text{(strength, bending-dominated),} \quad (6)$$

The parameter a is a direct indication of the loading efficiency of the structure at low relative densities, *i.e.* the higher the value of a, the more load the lattice can bear at a given relative density. The second term, $(1-a)\left(\frac{\rho}{\rho_s}\right)^m$, is an empirical power law that accounts for any change in deformation mode or importance of strut deformation to the lattice properties as the relative density progresses to higher values.

Using the simulation data, the semi-empirical trends of Eq. (3) – (6) were plotted as solid lines in Figure 2. The fitted parameters are listed in Table 2. As expected, the Simple Cubic and Octet Truss lattices behaved as stretch-dominated lattices with n = 1 at low relative densities. The fitted values of a for the relative moduli of Simple Cubic and Octet Truss are 0.41 and 0.17, respectively, which agree well with the analytically derived values of ~ 0.33 and 0.11 [8,31]. This result indicates that the Simple Cubic lattice was thrice as efficient in bearing load as the Octet Truss design, which, as discussed above, is a direct result of the Simple Cubic lattice having ~ 1/3 of its solid volume aligned to the loading axis. Similarly, Kelvin Cell lattices followed the expected behaviour of bending-dominated lattices at low relative densities ($\rho/\rho_s \leq 0.3$), with n = 2 and n = 1.5 for modulus and strength, respectively (Figure 2C and 2F).

Table 2: Values of parameters from Eq. 3-6 fitted to simulation data in Figure 2

Type	Parameter	**Simple Cubic**	**Octet Truss**	**Kelvin Cell**
Modulus	a	0.41	0.17	-
	m	2.40	2.80	2.00
Strength	a	0.12	0.03	0.03
	m	5.00	5.80	4.10

As the relative density increased beyond 0.3, however, its scaling relationship with the relative modulus and relative strength changed. Plotting the contributions of strut deformation (first term in Eq. (1) – (6)) and joint deformation (second term in Eq. (1) – (6)) in Figure 2 as

dotted and dashed lines, respectively, it becomes clear that this alteration in the scaling law reflects the increasing importance of joint deformation over strut deformation in influencing the lattice properties at high relative densities ($\rho/\rho_s > 0.3$). This is to be expected, since the joint volume was maintained at d^3 (d is the strut diameter), while the strut volume decreased proportionally with the strut length (l) at higher relative densities. Therefore, the proportion of solid in the joints dominates with increasing relative density and the lattice behaviour transitioned from 'strut-dominated' to 'joint-dominated'. The approximate point of this transition is marked with a "x" in Figure 2.

An exception to the above discussion can be found in Figure 2C, where the scaling law for the relative modulus of Kelvin Cell lattices remained unchanged for the entire range of relative density. However, previous analyses [32] have shown that this is because the elastic lattice behaviour of bending-dominated designs under joint influence at large relative density follows the same scaling law as that under strut influence at low relative density (*i.e.* $m = 2$), so that Eq. (5) simplifies to $\frac{E}{E_s} = \left(\frac{\rho}{\rho_s}\right)^2$ for $0 \leq \rho/\rho_s \leq 1$. Therefore, the result does not imply that strut-to-joint transition was absent for the Kelvin Cell lattices. Note, also, that we have not been able to fabricate and test Kelvin Cell lattices with $\rho/\rho_s > 0.3$, as the design rapidly approached a closed-cell geometry, which belongs to a different topology.

Furthermore, from Table 2, it can be observed that the values of a were much smaller for relative strength than for relative modulus, regardless of the lattice topology. This result suggests that the compressive strength of the lattices was governed mainly by the joint volume, even at low relative densities. In addition, it was found that $a = 0.03$ and $a = 0.12$ for the strength of the Octet Truss and Simple Cubic lattices respectively, which were much smaller than the expected value of 0.33 for stretch-dominated structures [8]. Similarly, the value of a for the strength of bending-dominated Kelvin Cell was an order of magnitude smaller than

other structures of the same topology [32]. To investigate this discrepancy, we conducted finite element simulations of the lattice deformations and found that, in all cases, the tensile stresses in the lattices reached alumina's tensile limit (300 MPa) before the compressive stresses rose to its compressive strength (2300 MPa). This implies that the lattices failed by tension rather than compression, despite being subjected to compressive loading. This was contrary to Ashby's analysis, which expected the lattices to fail because of excessive compressive stresses in the struts, and that would have been the more likely case, if not for the anisotropy in alumina's tensile (300 MPa) and compressive strength (2300 MPa). The failure behavior of the different lattices is discussed in more detail in the following sections.

3.2. Failure behaviour of Simple Cubic Lattices

Figure 3A shows the representative compressive stress-strain curve for Simple Cubic alumina microlattices (ρ/ρ_s = 0.4), along with corresponding images of the collapse process. Instead of a catastrophic failure commonly observed in solid ceramics, the ceramic lattices exhibited ~ 0.4% pseudoplastic strain before complete collapse at an overall failure strain of 1.2%. Such fracture behaviour closely resembles that of long-fibre-reinforced ceramic matrix composites, which produced the pseudoplasticity through the breaking and pull-out of fibres. In the case of the alumina microlattices, however, the pseudoplasticity originated from the sequential failure of the joints and struts (Figure 3A(i-v)), which involved the fracture and violent expulsion of the struts from the main lattice body as the elastic strain energy was being released. This process was always observed to proceed from the outer edges of the Simple Cubic microlattice towards the centre. Such fracture behavior has been observed commonly in the lattices with different relative densities.

Examining the von Mises stress distribution of the Simple Cubic microlattices in the simulations (insets of Figure 2A and 2D), it can be observed that the load was mainly supported through the axial compression of vertically aligned struts. However, as established in the previous section, the lattices failed because of the presence of tension, and therefore, the regions of the lattices with large tensile principal stresses are highlighted in Figure 3B-E. The lattices in Figure 3B and 3D were subjected to clamped-clamped boundary conditions at the top and bottom (*i.e.* positions of boundaries were fixed), while those in Figure 3C and 3E were subjected to roller-roller boundary conditions (*i.e.* horizontal positions of boundaries were not fixed).

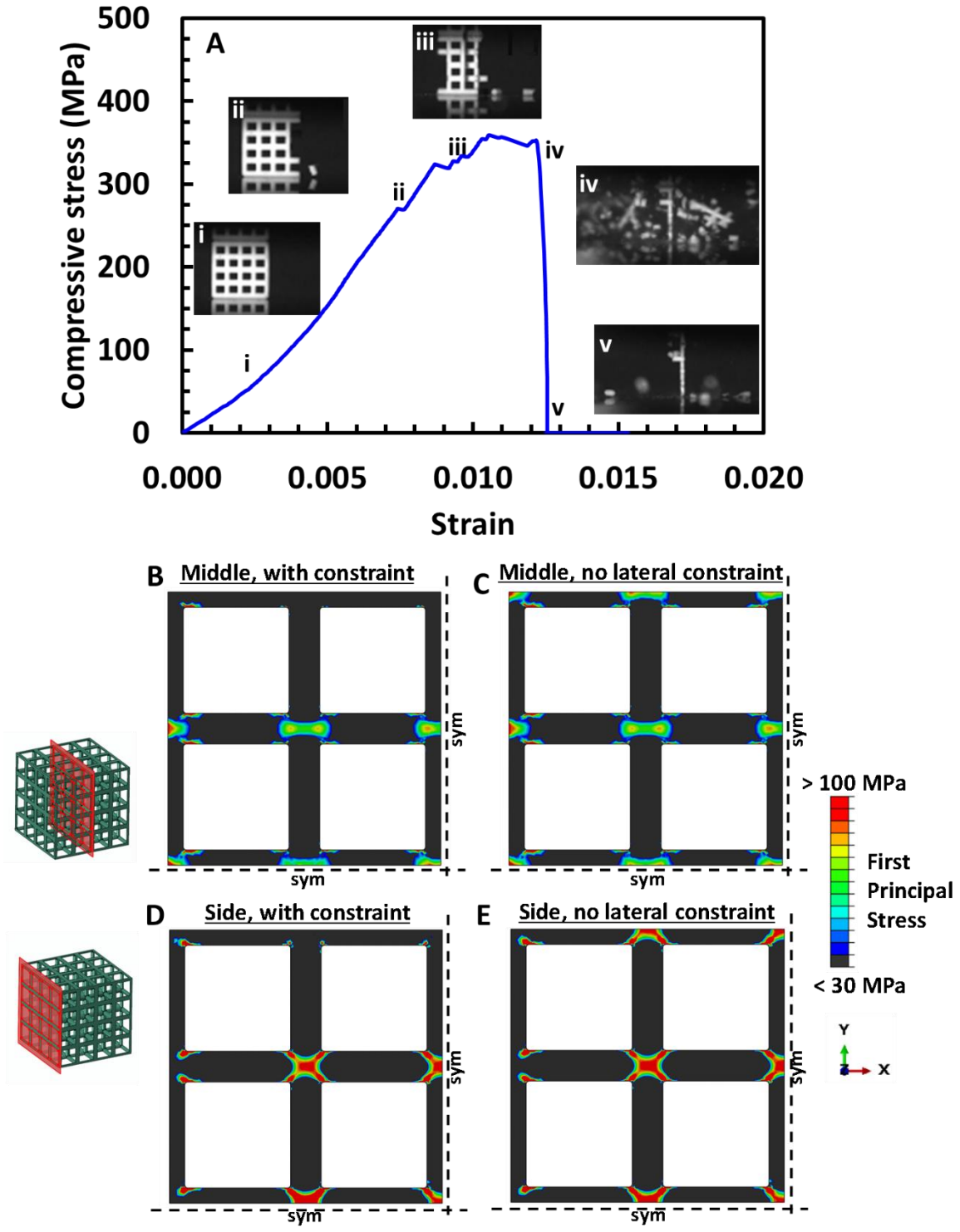

Figure 3: (A) Stress-strain curve of alumina Simple Cubic lattice (ρ/ρ_s = 0.4). (i) – (v) insets in (A) are the still frames from the high-speed video capture of the compression test moments. The loading direction was from top to bottom. (B-E) Regions of high First Principal Stress (*i.e.* tensile principal stress) are shown in a cross-sectional slice taken from the middle and the side of a simulated lattice (ρ/ρ_s = 0.1) right before the onset of failure. Compression was applied downwards on the top surface in the negative Y-direction and the effect of lateral constraints on the top and bottom surfaces of the lattice was compared.

In both cases, significant tension was present in the joints, as a result of the vertical struts indenting into the horizontal struts, causing by the Poisson's effect (*i.e.* the lateral dimension of a material stretches outwards as it is being compressed vertically). Therefore, the ends of the horizontal struts were particularly susceptible to fracture formation and propagation. This is supported by the observation that the lattice debris contained many full-length struts that had fractured at the joints (see Figure 3A(ii, iii)).

The concentration of the principal tensile stresses was more severe at the free edges along the sides of the lattice (Figure 3D, E), where the joints were subjected to asymmetric forces and moments, than in the middle region (Figure 3B, C). It is, therefore, not surprising to observe that the failure of the Simple Cubic lattice began with the fracture of struts on the outermost edges (Figure 3A(ii)) and proceeding inwards (Figure 3A(iii)), until only the middle vertical strut was left standing before complete structural breakdown (Figure 3A(iv-v)). In addition, although most of the fractures cut through the joints, there were also instances when the fractures were found to propagate down the middle of the vertical struts as well (Figure S4 in Supplementary Material), which is induced the uniaxial compressive loading. It is also interesting to note that the presence of lateral constraints on the top and bottom surface of the lattice had no significant impact on the failure process of Simple Cubic lattices, as evidenced by a comparison of Figure 3B and 3D with Figure 3C and 3E. This behaviour is totally different from that of Octet Truss lattice and Kelvin Cell lattices, as will be elaborated in next sections.

3.3. Failure behaviour of Octet Truss Lattices

Figure 4A and Figure 4B shows the representative stress-strain curves of alumina Octet Truss lattices for $\rho/\rho_S = 0.15$ and $\rho/\rho_S = 0.5$, respectively. Still frames corresponding to different points on the curves are shown in Figure 4A(i –v) and Figure 4B(i – v). Similar to the Simple

Cubic lattices, the lattices exhibited ~ 0.2% - 0.3% of pseudoplastic strain due to the successive fracture of struts.

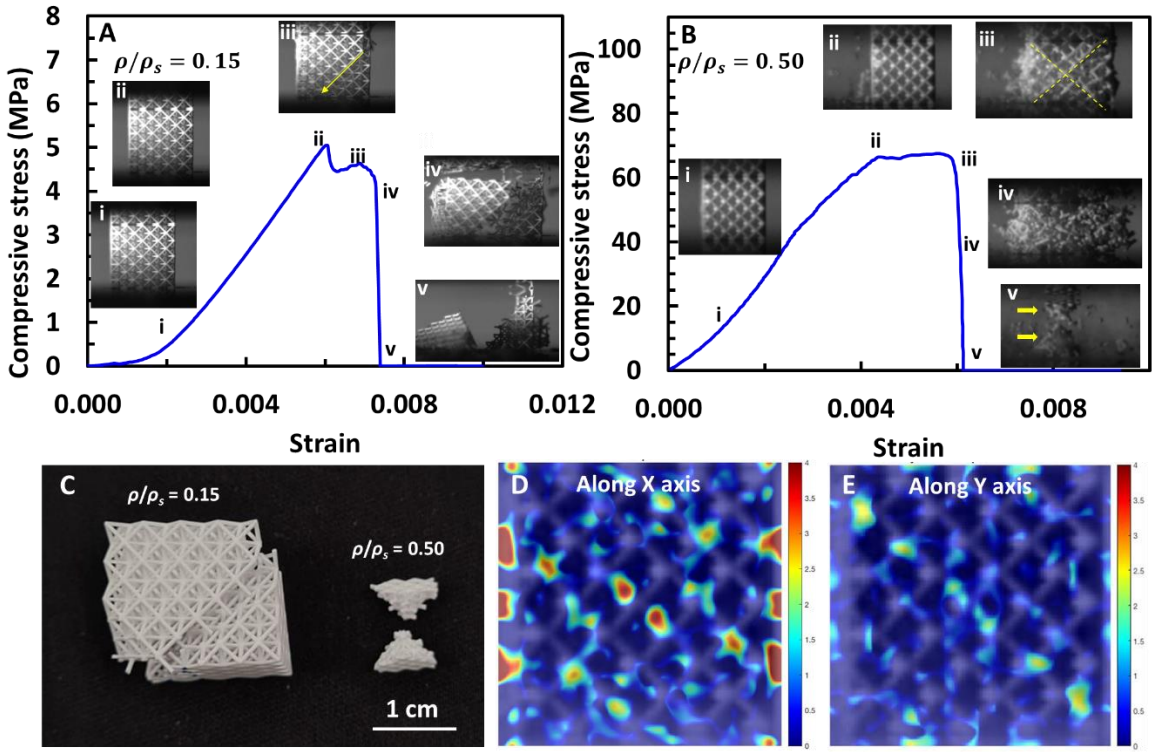

Figure 4: (A) Stress-strain curve of alumina Octet Truss lattice (ρ/ρ_s = 0.15). (i) – (iv) Still frames from the high-speed video capture of the compression testing. The loading direction is from top to bottom. (B) Stress-strain curve of alumina Octet Truss lattice (ρ/ρ_s = 0.5). (i) – (v) Still frames from the high-speed video capture of the compression testing. The loading direction was from top to bottom. （C）Photo of two fragments found in the ρ/ρ_s = 0.15 and 0.50 lattice after compression. (D-E) Maps of displacement in the ρ/ρ_s = 0.50 lattice along the X- (D) and Y- axis (E) right before catastrophic collapse occurred. Note the map is relative displacement map.

For Octet Truss lattices with $\rho/\rho_s \leq$ 0.3, the structures underwent linear, elastic deformation until the peak stress was reached (Figure 4A(i-ii)). Beyond this, some struts began to fracture, as seen from the slight drop in the stress sustained by the lattice (Figure 4A(ii-iii)). Further compression caused the entire lattice to split along a (110) plane suddenly (yellow line in Figure 4A(iii)), as the top half of the lattices shifted and detached itself from the bottom half of the lattice (Figure 4A(iii-iv). The two split parts of the lattice are shown in Figure 4C (left).

In contrast, for Octet Truss lattices with $\rho/\rho_s > 0.3$, the tangent modulus was observed to decrease with increasing strain after a similar linear elastic deformation at first (Figure 4B(i)). As the stress approached the peak (Figure 4B(ii)), a few struts were ejected from the side of lattice occasionally, but the lattice maintained most of its structural integrity. Following a short stress plateau, a sudden catastrophic failure of large parts of the lattice, resembling an explosion occurred (Figure 4B(iii)-(v)). A closer examination of the high-speed video capture (Figure 4B(iii)) showed that the lattice failure was divided along the (110) plane (indicated by a yellow 'X' in Figure 4B(iii)). Displacement maps of the lattice right before catastrophic failure, generated using the Graphic Phase Analysis method [25–27], show that the centre layer of the lattice had a much larger displacement along the *X*-axis, especially in the outermost regions, than the top and bottom regions (Figure 4D). Struts along one of the (110) plane also exhibited excess strain in the *Y*-axis (Figure 4E). Consequently, the regions of the lattice to the left and right of the 'X' in Figure 4B(iii) fractured explosively, but the top and bottom pyramids of the lattice remained intact, which is clear from the remnants of the lattice (see Figure 4B(v) and Figure 4C(right)).

Based on the principal stress distribution obtained from finite element simulations (Figure 5A-D), it becomes clear that (i) fracture in the lattices was mostly initiated at the ends of the horizontal struts, which were under relatively high tensile stress and (ii) the divide along the (110) plane (indicated by the yellow dashed line in Figure 5A) occurred because of the fixed boundary conditions applied to the top and bottom of the lattices. Constrained by the friction from the compression platens, horizontal struts near the top and bottom edges of the lattices were not allowed to deform as much, and thus, were subjected to smaller tensile stresses (Figure 5A). This boundary effect was reduced for struts that were farther away from the fixed top and bottom edges (Figure 5A), as well as for those that were closer to the free edges along the lattice sides, which gave them room for deformation (Figure 5C). As a result, two distinct

regions were formed within the Octet Truss lattice – horizontal struts that were found within the pyramids, which start from the fixed top and bottom edges and tapered towards the center, experienced smaller tensile principal stresses than horizontal struts outside of these zones. This spatial division was observed in the simulations for all Octet Truss geometries investigated here ($0.1 < \rho/\rho_s < 0.5$), however, not observed at all when the fixed boundary conditions were absent (Figure 5B and 5D).

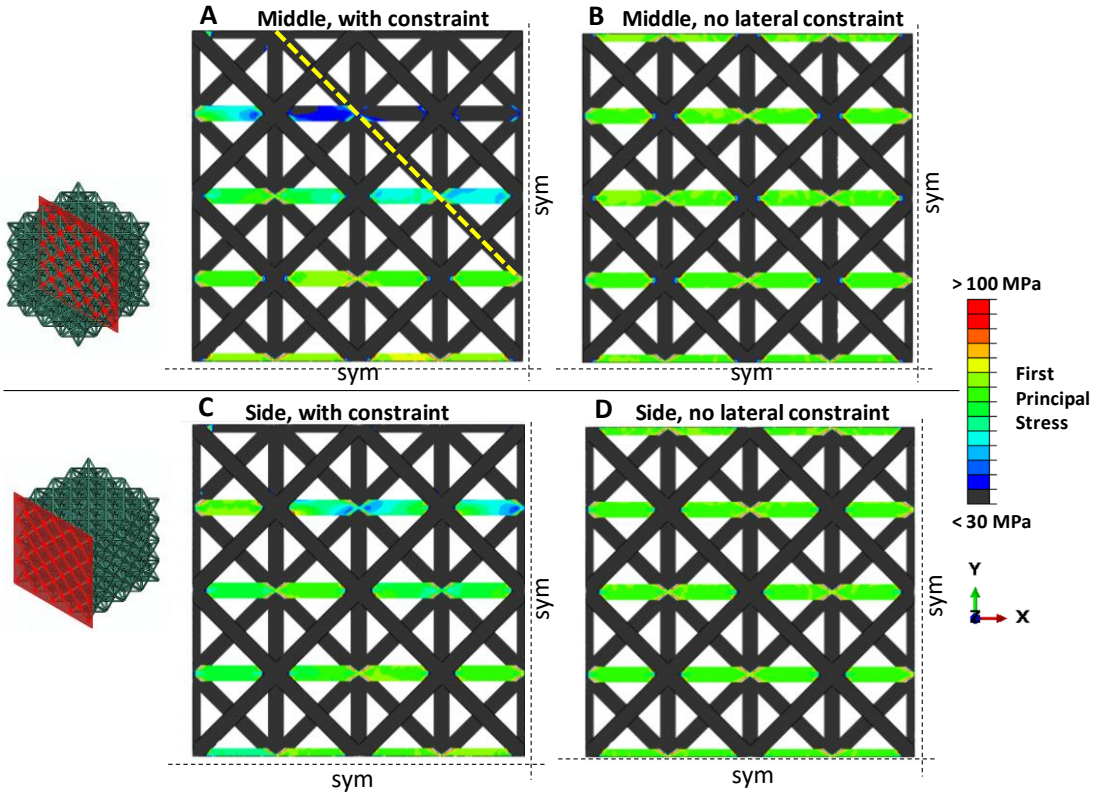

Figure 5: Regions of high First Principal Stress (*i.e.* tensile principal stress) taken from the middle and the side of a simulated lattice (ρ/ρ_s = 0.1) right before the onset of failure, with lateral constraint (A, C) and without constraint (B,D). Compression was applied downwards on the top surface in the negative Y-direction and the effect of lateral constraints on the top and bottom surfaces of the lattice was compared.

Based on the above analysis, it is, therefore, unexpected that the pyramidal regions remained intact while the rest of the lattice failed catastrophically at the same time, which was observed for Octet Truss lattices with $\rho/\rho_s > 0.3$. For the lattices with small relative densities ($\rho/\rho_s \leq 0.3$), strut fracture appeared to progress more sequentially and less violently, with the

process ending when the lattice split into 2 major parts along the (110) plane, rather than complete pulverization of any material outside of the pyramids.

One plausible explanation for this dichotomy could be that the high aspect ratio struts in low relative density lattices were susceptible to failure through buckling, in addition to the expected failure through tension at the joints. Therefore, if any one of the struts along the highly stressed (110) plane was fractured and lost, the load would be passed on to the rest of the struts in the plane which would fail progressively through buckling, much like how buckling of a single polymeric strut in a Simple Cubic lattice can cause the whole layer of struts to buckle consequently [33]. Once the lattice was split along its diagonal, load transfer between the two halves would no longer be possible and thus, no further failure of the lattice was observed. On the other hand, the low aspect ratio struts in high relative density lattices could not fail by buckling, as the critical stress for inducing buckling would be much higher than the maximum tensile stress they can sustain. As a result, the tension in these struts continued to build until it was released simultaneously by fracturing. Those struts subjected to higher tensile stress (e.g. outside the pyramidal region and near side surface) fractured together explosively.

3.4. Failure behaviour of Kelvin Cell Lattices

Figure 6A shows the representative stress-strain curves of the Kelvin Cell lattice for $\rho/\rho_s = 0.15$. Still frames corresponding to different points on the curves are shown in the insets of Figure 6A(i –vi). Similar to the Simple Cubic lattice and Octet Truss lattice, Kelvin Cell lattices exhibited ~ 0.36% pseudoplastic strain, followed by a catastrophic fracture.

Plotting the tensile principal stress distribution in Figure 6B-E, it was found that fixed boundary conditions at the top and bottom edges of the lattice generated large stress concentrations in the joints that laid in the (110) planes (indicated by yellow dashed lines in

Figure 6B and 6D). If lateral constraints at the top and bottom edges were absent (*i.e.* no friction between lattice and platen), as shown in Figure 6C and 6E, there would be no elevated tensile stresses in the joints along the (110) plane.

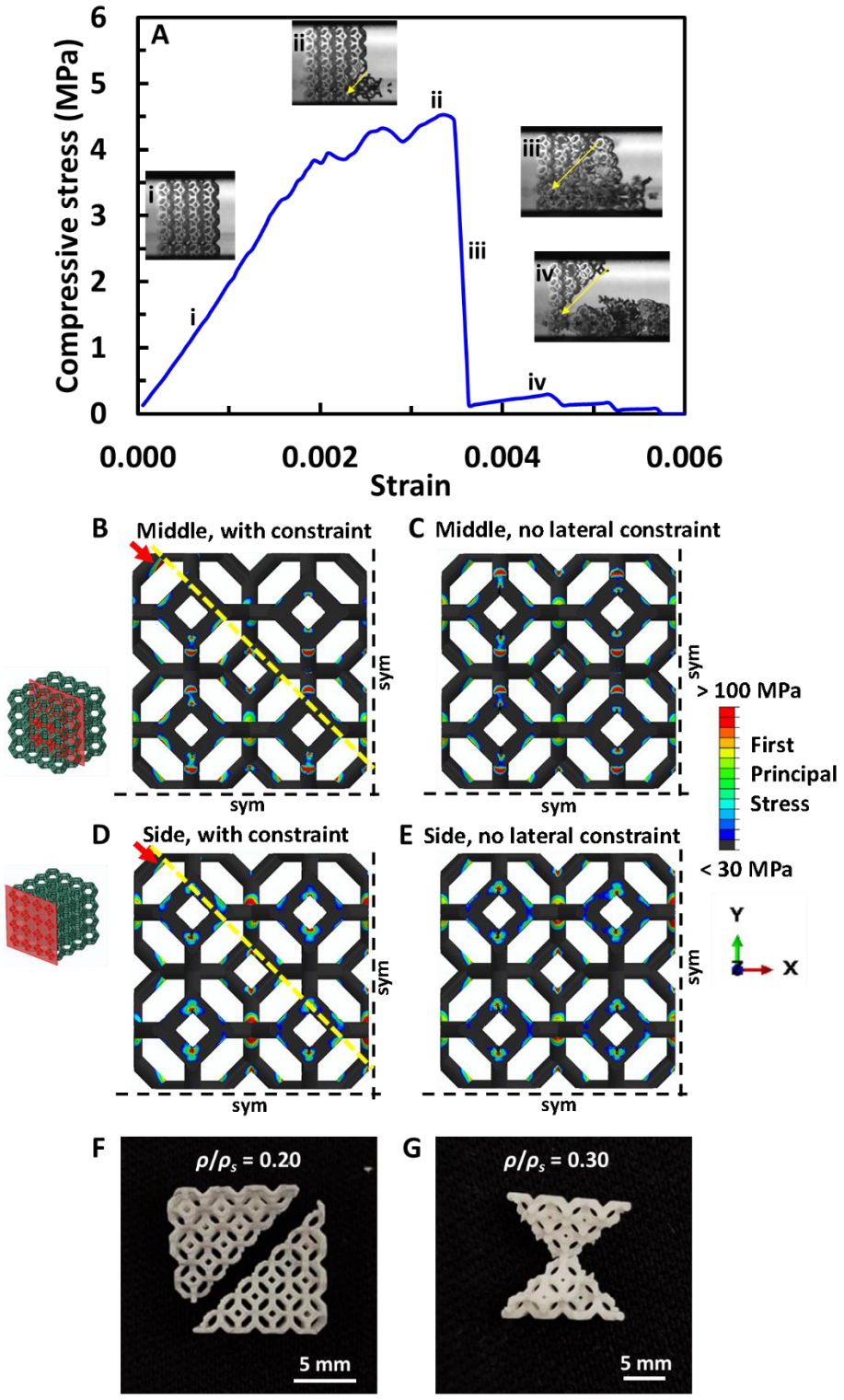

Figure 6: (A) Stress-strain curve of alumina Kelvin Cell lattice (ρ/ρ_s = 0.15). (i) – (iv) Still frames from the high-speed video capture of the compression testing. The loading direction was from top to bottom. (B-E) Regions of high First Principal Stress (*i.e.* tensile principal stress) taken from the middle and the side of a simulated lattice (ρ/ρ_s = 0.1) right before the onset of failure. Compression was applied downwards on the top surface in the negative Y-direction and the effect of lateral constraints on the top and bottom surfaces of the lattice was compared. (F-G) Photos of a Kelvin Cell with ρ/ρ_s = 0.2 (F) and ρ/ρ_s = 0.3 (G) after fracture.

As a result of these stresses, fracture of the low relative density alumina Kelvin Cell lattice began at one of the fixed edges (bottom edge, for the case shown in Figure 6A(i-vi)) and progressively chipped away at the lattice along the (110) plane, which contributed to its pseudoplasticity. The failure process ended when half of the lattice along the diagonal became damaged and the lattice was unable to bear any more load (Figure 6A(iii-iv). Figure 6F shows an example of lattice fragments after the lattices collapsed. Similar to the Octet Truss design, this successive fracture of the struts gave way to a more spontaneous failure along the (110) planes when ρ/ρ_s was increased to 0.3, so that only pyramidal fragments at the top and bottom of the Kelvin Cell lattices were left intact (Figure 6G). Once again, this was most likely because high aspect ratio struts in low relative density lattices were more susceptible to failure by buckling, while the low aspect ratio struts in high relative density lattices were more likely to fail by tensile stress build-up. Fractures along the (110) planes for both Octet Truss and Kelvin Cell had also been observed previously with porous alumina lattices coated with silicon carbide [17].

4. DISCUSSION

4.1 *Comparison with Ductile Lattices*

Comparing the mechanical responses of the brittle alumina microlattices and those fabricated out of ductile materials, certain similarities can be drawn. Firstly, the dependence of the relative modulus and relative strength on the relative density for both types of lattices follow Ashby's power laws reasonably well for $\rho/\rho_s \leq 0.3$. Secondly, ductile Octet Truss and Kelvin Cell lattices have also been observed to fail along diagonal planes, through the development of shear bands [4][34]. This is because the boundary conditions applied to the top and bottom edges of the ductile lattices during compressive testing were the same as those for the alumina

lattices. Furthermore, there is also a similar change in failure behaviour when the relative density of ductile lattices increased beyond a certain threshold. For instance, large localized strain tend to form along diagonal planes for low relative density Octet Truss lattices, while uniform buckling of struts across the entire lattice was more characteristic of the failure for large relative density lattices [11,35]. Thirdly, the alumina microlattices exhibited a pseudoplastic behaviour, where the peak stress was sustained for a limited amount of strain, similar to the "plateau stress" regime in ductile lattice deformation. Both of the strains originated from the successive deformation or fracture of struts.

On the other hand, there are several striking differences as well. For instance, the strength of the alumina lattices at low relative densities were an order of magnitude lower than that predicted by Ashby's analysis. We have ascertained that this is because additively manufactured alumina, like many other ceramics, fail at a tensile stress (0.3 GPa) that is an order of magnitude lower than that for compression (2.3 GPa). When local regions of tension developed as the microlattices were compressed (Fig. 3B & D, 5C, and 6D), fractures initiated in the lattices due to these tensile stresses. Fig. 3B, 3D, 5C and 6D also show that tensile stresses were most dominant at the boundaries of the microlattices, due to free edge effects *i.e.* movement of the trusses at the boundaries were less constrained. In contrast, Ashby's analysis assumed that fractures would only develop when alumina reached its compressive limit (2.3 GPa) instead of tensile limit (0.3 GPa), leading to an overestimation of the lattice strength.

In addition, while ductile struts can yield and deform plastically to maintain the topology of a lattice and continue bearing load, the inherent brittleness of ceramic struts causes them to fracture and become lost to the lattice upon failure. As a result, unlike ductile lattices, the alumina microlattices did not exhibit a densification stage during compression, where the air spaces in a lattice had been completely squeezed out, leaving only the constituent material. The densification stage is characterized by a rapid rise in the overall stress borne by the lattice.

Instead, for the alumina microlattices, the effective stress plunged to ~ 0 immediately after ultimate failure (Figure 3, 4 and 6).

Furthermore, the strain at plateau stress exhibited by the ceramic lattices before this ultimate failure was highly limited (~ 0.1 % - 0.5 %) compared to that of ductile metal and polymer lattices (~ 5 – 50 %) [4,36]. The pseudoplasticity exhibited by the ceramic lattices came from their ability to break up fracture propagation paths, due to the porous nature of their geometry, so that all the struts in the lattices did not fail simultaneously. However, because the struts were still interconnected through the joints, there remained limited resistance to crack propagation, evidenced by the long cracks that travelled straight down the middle of vertical struts in the Simple Cubic lattices (see Figure S4 in Supplementary Material). In contrast, polymeric Simple Cubic lattices had previously been observed to exhibit plateau stresses that extended up to 60% strain, by failing in a layer-by-layer manner through extensive plastic buckling of the vertical struts [33]. Nevertheless, the pseudoplasticity exhibited by the alumina microlattices, limited as it may be, allows these ceramic structures to accommodate small dimensional changes in mated parts due to, say, thermal cycling, and also, provide warning signs before catastrophic failure, which solid ceramics are unable to do (refer to Figure S2 in Supplementary Material).

4.2 Comparison with Current Materials

In spite of the brittle failure behaviour, alumina microlattices offer a unique combination of chemical inertness, high thermal stability and outstanding mechanical properties that cannot be easily replaced by ductile metal or polymeric lattices. For instance, the stiffness of the alumina Octet Truss microlattices was 5 times better than that fabricated

from Maraging steel [4] and 260 times better than that of polymeric lattices [12] at the same relative densities.

A more comprehensive evaluation can be found in Figure 7A, where the moduli of the alumina microlattices are compared against those of current materials. It is clear from the plot that the alumina microlattices had relatively high specific stiffnesses, particularly, the Simple

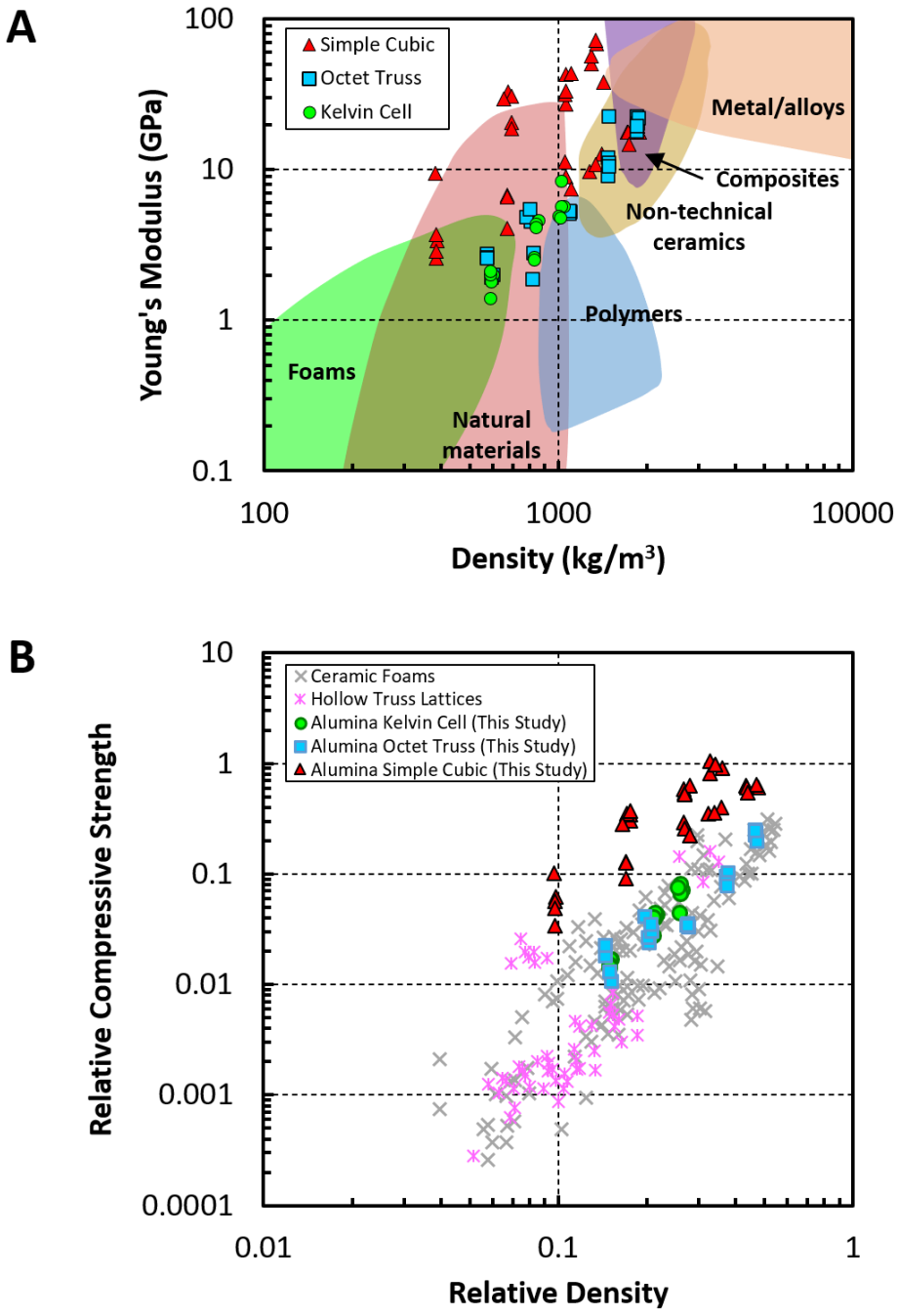

Figure 7: (A) Ashby chart of Young's modulus against density for the alumina microlattices. (B) Plot of relative compressive strength vs. relative density for the alumina microlattices (this study), hollow-truss metal oxide lattices and ceramic foams in the literature [37,38]. In order to compare our data fairly with those in the literature, the relative compressive strength was computed following the format in these prior studies [37,38], where the compressive strength was normalized with the flexural strength of the constituent material of the lattices (*i.e.* tensile strength is taken as the σ_s). Since the tensile limit of a ceramic is smaller than its compressive limit, the value of the relative compressive strength here can exceed 1. For relative strength values of the alumina microlattices where the compressive limit of solid alumina was taken as σ_s, please refer to Figure 2. The theoretical maximum represents the Voigt bound *i.e.* σ_c/σ_{ts} =

$(\rho/\rho_s)(\sigma_{cs}/\sigma_{ts})$. σ_c – compressive strength of lattice; σ_{cs} – compressive strength of alumina; σ_{ts} – tensile strength of alumina.

Cubic structures, which exhibited values (~ 40–70 GPa) that had not been demonstrated before in the density range of 1.0 – 1.43 kg/m^3 (*i.e.* data points in the white space). Moreover, a large number of the lattices also showed specific moduli that are in the upper range of values for foams, natural materials and polymers. With the added advantages of high temperature stability, corrosion resistance and low thermal expansion coefficient, alumina microlattices are potentially an effective substitute for some of these materials, particularly for operations in harsh environments.

Besides the advantages derived from the inherent properties of alumina, the microlattices were also rationally designed for load bearing, as well as energy absorption, and they were fabricated using stereolithography 3D printing process that allowed complete control over the entire geometry. Architected materials such as these can naturally be expected to perform better than ceramic foam structures that rely on stochastic processes, such as foaming techniques [39–41], which is clear from Figure 7B. The alumina microlattices were also observed to perform better than Simple Cubic hollow-strut metal oxide lattices (pink cross data in Figure 7B), likely because the fabrication process in this case allowed for better shaping control than the dip-coating method used previously, and the presence of joints in the solid strut geometry resisted loads better than the hollow-strut design [37].

These results are remarkable, considering that the lattice designs and fabrication process can be further optimized. For instance, our analysis indicates that failure in all the geometries investigated here is initiated in the joints. In addition, the layer-by-layer production of the 3D printing process and subsequent debinding/sintering processes can lead to significant surface roughness (see Figure S1 in Supplementary Material) and even misalignment in

between layers (Figure S5 in Supplementary Material). The uneven surfaces can degrade the mechanical properties of the lattices as ceramic fracture is usually initiated at surface defects. When the edges of lattices were misaligned (Figure S5), the mechanical properties were also degraded. For instances, the compressive strength of a slanted Simple Cubic lattice was found to drop by ~20%, and Young's modulus was reduced by ~60 %. Therefore, it may be possible to improve the mechanical properties of the alumina microlattices even further, if the design of the joints is modified, for instance, through filleting, and post-fabrication steps such as polishing are employed to reduce surface roughness and misalignments.

5. CONCLUSIONS

In this work, the mechanical properties and failure behaviour of Simple Cubic, Octet Truss and Kelvin Cell geometries have been studied through experiments and numerical simulation. It was found that the modulus and strength of the alumina microlattices followed Ashby's classic scaling law well at low relative densities, although the absolute values of the compressive strength were an order of magnitude lower than predicted. Our results indicate that this deviation was because the microlattices failed by tension, which the constituent alumina is less resistant to, compared to compressive stress. These regions of tension could not be eliminated in the lattice, regardless of design, and despite it being under an overall compressive load.

In addition, at low relative density (≤ 0.3), the alumina microlattices failed by sequential localized fracture while at high relative density, they failed mainly through simultaneous fracture. The transition was caused by a decrease in the struts' susceptibility to buckling at higher relative densities (*i.e.* lower aspect ratios of the struts). For the Simple Cubic geometry, fracture occurred column-by-column from the sides inwards to the centre, while fracture of the

Octet Truss and Kelvin Cell lattices usually initiated and proceeded along the diagonal (110) plane.

Comparison with existing materials shows that the alumina microlattices possessed excellent specific modulus and specific strength. They also displayed limited ductility in the form of ~ 0.1 % - 0.5 % of pseudoplastic strain, which would allow them to accommodate small tolerance changes and provide warning before catastrophic failure.

ACKNOWLEDGEMENTS

The authors would like to acknowledge with thanks the financial support of the work by A*STAR AME IRG grant with project number of A1883c0009 and the project with PA number of POD0713727.

DATA AVAILABILITY

The raw/processed data required to reproduce these findings cannot be shared at this time due to technical or time limitations.

REFERENCES

[1] Schaedler TA, Jacobsen AJ, Torrents A, Sorensen AE, Lian J, Greer JR, et al. Ultralight Metallic Microlattices. Science 2011;334:962–5. https://doi.org/10.1126/science.1211649.

[2] Meza LR, Zelhofer AJ, Clarke N, Mateos AJ, Kochmann DM, Greer JR. Resilient 3D hierarchical architected metamaterials. PNAS 2015;112:11502–7. https://doi.org/10.1073/pnas.1509120112.

[3] Meza LR, Das S, Greer JR. Strong, lightweight, and recoverable three-dimensional ceramic nanolattices. Science 2014;345:1322–6. https://doi.org/10.1126/science.1255908.

[4] Al-Ketan O, Rowshan R, Abu Al-Rub RK. Topology-mechanical property relationship of 3D printed strut, skeletal, and sheet based periodic metallic cellular materials. Additive Manufacturing 2018;19:167–83. https://doi.org/10.1016/j.addma.2017.12.006.

[5] Deshpande VS, Fleck NA, Ashby MF. Effective properties of the octet-truss lattice material. J Mech Phys Solids 2001;49:23.

[6] Arabnejad S, Burnett Johnston R, Pura JA, Singh B, Tanzer M, Pasini D. High-strength porous biomaterials for bone replacement: A strategy to assess the interplay between cell morphology, mechanical properties, bone ingrowth and manufacturing constraints. Acta Biomaterialia 2016;30:345–56. https://doi.org/10.1016/j.actbio.2015.10.048.

[7] Peng C, Tran P, Nguyen-Xuan H, Ferreira AJM. Mechanical performance and fatigue life prediction of lattice structures: Parametric computational approach. Composite Structures 2020;235:111821. https://doi.org/10.1016/j.compstruct.2019.111821.

[8] Ashby MF. The properties of foams and lattices. Philosophical Transactions of the Royal Society A: Mathematical, Physical and Engineering Sciences 2006;364:15–30. https://doi.org/10.1098/rsta.2005.1678.

[9] Khaderi SN, Deshpande VS, Fleck NA. The stiffness and strength of the gyroid lattice. International Journal of Solids and Structures 2014;51:3866–77. https://doi.org/10.1016/j.ijsolstr.2014.06.024.

[10] Mazur M, Leary M, McMillan M, Sun S, Shidid D, Brandt M. 5 - Mechanical properties of Ti6Al4V and AlSi12Mg lattice structures manufactured by Selective Laser Melting (SLM). In: Brandt M, editor. Laser Additive Manufacturing, Woodhead Publishing; 2017, p. 119–61. https://doi.org/10.1016/B978-0-08-100433-3.00005-1.

[11] Tancogne-Dejean T, Spierings AB, Mohr D. Additively-manufactured metallic micro-lattice materials for high specific energy absorption under static and dynamic loading. Acta Materialia 2016;116:14–28. https://doi.org/10.1016/j.actamat.2016.05.054.

[12] Ling C, Cernicchi A, Gilchrist MD, Cardiff P. Mechanical behaviour of additively-manufactured polymeric octet-truss lattice structures under quasi-static and dynamic compressive loading. Materials and Design 2019;162:106–18. https://doi.org/10.1016/j.matdes.2018.11.035.

[13] Zheng X, Lee H, Weisgraber TH, Shusteff M, DeOtte J, Duoss EB, et al. Ultralight, ultrastiff mechanical metamaterials. Science 2014;344:1373–7.

[14] Bauer J, Crook C, Guell Izard A, Eckel ZC, Ruvalcaba N, Schaedler TA, et al. Additive Manufacturing of Ductile, Ultrastrong Polymer-Derived Nanoceramics. Matter 2019;1:1547–56. https://doi.org/10.1016/j.matt.2019.09.009.

[15] Eckel ZC, Zhou C, Martin JH, Jacobsen AJ, Carter WB, Schaedler TA. Additive manufacturing of polymer-derived ceramics. Science 2016;351:58–62.

[16] Vyatskikh A, Kudo A, Delalande S, Greer JR. Additive manufacturing of polymer-derived titania for one-step solar water purification. Materials Today Communications 2018;15:288–93. https://doi.org/10.1016/j.mtcomm.2018.02.010.

[17] Mei H, Zhao R, Xia Y, Du J, Wang X, Cheng L. Ultrahigh strength printed ceramic lattices. Journal of Alloys and Compounds 2019;797:786–96. https://doi.org/10.1016/j.jallcom.2019.05.117.

[18] Cui H, Hensleigh R, Chen H, Zheng X. Additive Manufacturing and size-dependent mechanical properties of three-dimensional microarchitected, high-temperature ceramic metamaterials. Journal of Materials Research 2018;33:360–71. https://doi.org/10.1557/jmr.2018.11.

[19] Zhang X, Vyatskikh A, Gao H, Greer JR, Li X. Lightweight, flaw-tolerant, and ultrastrong nanoarchitected carbon. PNAS 2019;116:6665–72. https://doi.org/10.1073/pnas.1817309116.

[20] Crook C, Bauer J, Izard AG, Oliveira CS de, Silva JM de S e, Berger JB, et al. Plate-nanolattices at the theoretical limit of stiffness and strength. Nat Commun 2020;11:1–11. https://doi.org/10.1038/s41467-020-15434-2.

[21] Bauer J, Schroer A, Schwaiger R, Kraft O. Approaching theoretical strength in glassy carbon nanolattices. Nature Materials 2016;15:438–43. https://doi.org/10.1038/nmat4561.

[22] Bauer J, Meza LR, Schaedler TA, Schwaiger R, Zheng X, Valdevit L. Nanolattices: An Emerging Class of Mechanical Metamaterials. Advanced Materials 2017;29:1701850. https://doi.org/10.1002/adma.201701850.

[23] Cui H, Hensleigh R, Chen H, Zheng X. Additive Manufacturing and size-dependent mechanical properties of three-dimensional microarchitected, high-temperature ceramic metamaterials. Journal of Materials Research 2018;33:360–71. https://doi.org/10.1557/jmr.2018.11.

[24] 3DCERAM. 3Dmix Alumina Technical Datasheet n.d.;33:16062016.

[25] Qi L, He S, Chen C, Jiang B, Hao Y, Ye H, et al. Diffusional-displacive transformation in a metastable β titanium alloy and its strengthening effect. Acta Materialia 2020. https://doi.org/10.1016/j.actamat.2020.05.058.

[26] Hÿtch MJ, Putaux J-L, Pénisson J-M. Measurement of the displacement field of dislocations to 0.03 Å by electron microscopy. Nature 2003;423:270–3. https://doi.org/10.1038/nature01638.

[27] Seo S, Noh H, Li N, Jiang J, Tarantini C, Shi R, et al. Artificially engineered nanostrain in FeSe x Te 1-x superconductor thin films for supercurrent enhancement. NPG Asia Materials 2020;12:1–11. https://doi.org/10.1038/s41427-019-0186-y.

[28] Abaqus documentation https://abaqus-docs.mit.edu/2017/English/SIMACAEMATRefMap/simamat-c-cracking.htm 2017.

[29] Khan AJ, Iqbal N, Saeed HA, Tarar WA. Development of material model for assessment of brittle cracking behavior of plexiglas. IOP Conf Ser: Mater Sci Eng 2016;146:012008. https://doi.org/10.1088/1757-899X/146/1/012008.

[30] Pelfrene J, Dam S, Sevenois R, Gilabert F, Van Paepegem W. Fracture Simulation of Structural Glass by Element Deletion in Explicit FEM. Challenging Glass 5 – Conference on Architectural and Structural Applications of Glass 2016.

[31] Deshpande VS;, Fleck NA;, Ashby MF. Effective properties of the octet-truss lattice material. Journal of Engineering Materials and Technology, Transactions of the ASME 2018;140:1747–69. https://doi.org/10.1115/1.4040409.

[32] Gibson LJ, Ashby MF. The Mechanics of Three-Dimensional Cellular Materials. Proceedings of the Royal Society A: Mathematical, Physical and Engineering Sciences 1982;382:43–59. https://doi.org/10.1098/rspa.1982.0088.

[33] Lai CQ, Daraio C. Highly porous microlattices as ultrathin and efficient impact absorbers. International Journal of Impact Engineering 2018;120:138–49. https://doi.org/10.1016/j.ijimpeng.2018.05.014.

[34] Bonatti C, Mohr D. Large deformation response of additively-manufactured FCC metamaterials: From octet truss lattices towards continuous shell mesostructures. International Journal of Plasticity 2017;92:122–47. https://doi.org/10.1016/j.ijplas.2017.02.003.

[35] Song J, Zhou W, Wang Y, Fan R, Wang Y, Chen J, et al. Octet-truss cellular materials for improved mechanical properties and specific energy absorption. Materials & Design 2019;173:107773. https://doi.org/10.1016/j.matdes.2019.107773.

[36] Latture RM, Rodriguez RX, Holmes LR, Zok FW. Effects of nodal fillets and external boundaries on compressive response of an octet truss. Acta Materialia 2018;149:78–87. https://doi.org/10.1016/j.actamat.2017.12.060.

[37] Kanaujia PK, bin Ramezan MA, Yap XY, Song Y, Du Z, Gan CL, et al. Mechanical response of lightweight hollow truss metal oxide lattices. Materialia 2019;8:100439. https://doi.org/10.1016/j.mtla.2019.100439.

[38] Studart AR, Gonzenbach UT, Tervoort E, Gauckler LJ. Processing Routes to Macroporous Ceramics: A Review. Journal of the American Ceramic Society 2006;89:1771–89. https://doi.org/10.1111/j.1551-2916.2006.01044.x.

[39] Han YS, Li JB, Chen YJ. Fabrication of bimodal porous alumina ceramics. Materials Research Bulletin 2003;38:373–9. https://doi.org/10.1016/S0025-5408(02)01026-7.

[40] Han Y, Li J, Wei Q, Tang K. The effect of sintering temperatures on alumina foam strength. Ceramics International 2002;28:755–9. https://doi.org/10.1016/S0272-8842(02)00039-1.

[41] Tallon C, Chuanuwatanakul C, Dunstan DE, Franks GV. Mechanical strength and damage tolerance of highly porous alumina ceramics produced from sintered particle stabilized foams. Ceramics International 2016;42:8478–87. https://doi.org/10.1016/j.ceramint.2016.02.069.